Eight-coordinate mono- and dinuclear Dy(II) complexes containing a rigid equatorial plane and an anisobidentate carboxylate ligand in the axial position: synthesis, structure and magnetism

Pankaj Kalita, Kusum Kumari, Pawan Kumar, Vierandra Kumar, Saurabh Kumar Singh, Guillaume Rogez, Vadapalli Chandrasekhar

Eight-Coordinate Mono- and Dinuclear Dy(III) Complexes Containing a Rigid equatorial plane and an Anisobidentate Carboxylate ligand in the Axial position: Synthesis, Structure and Magnetism.

Pankaj Kalita*,[a] Kusum Kumari,[b] Pawan Kumar,[c] Vierandra Kumar,[c] Saurabh Kumar Singh,*[b] Guillaume Rogez*[d] and Vadapalli Chandrasekhar*[c]

[a]Department of Chemistry, Nowgong Girls' College, Nagaon, Assam-782 002, India.

[b]Department of Chemistry, Indian Institute of Technology Hyderabad, Kandi, Sangareddy, Telangana-502 285, India.

[c]Tata Institute of Fundamental Research Hyderabad, Gopanpally, Hyderabad-500 107, India.

[d]Institut de Physique et Chimie des Matériaux de Strasbourg (IPCMS) CNRS/Université de Strasbourg, UMR 7504, 67000 Strasbourg, France.

*vc@tifr.res.in; Guillaume.Rogez@ipcms.unistra.fr; sksingh@chy.iith.ac.in;

pankajkalita976@gmail.com

ABSTRACT

A rigid pentadentate chelating ligand (H_2L) has been utilized to synthesize a series of octa-coordinate mononuclear complexes, [Dy(L)(Ph_3PO)(OOCR)] (where R = C_6H_5 (**1**), $C(CH_3)_3$ (**2**), CF_3 (**3**)) and a dinuclear complex, [$Dy_2(L)_2(Ph_3PO)_2\{(OOC)_2C_6H_4\}$] (**4**) based on the highly anisotropic Dy(III) ion. All the complexes are structurally characterized by single-crystal X-ray diffraction studies. The complexes are formed by the coordination action of the dianionic pentadentate ligand $[L]^{2-}$, one phosphine oxide, and the carboxylate ligands. DC and AC magnetic measurements were performed on **1**–**4**. Complexes **1**–**4** show SMM behaviour, under zero DC field for **1** and **4**, under 500 Oe and 1000 Oe DC field for **2** and **3** respectively, with thermally activated, Raman, and Raman and quantum tunneling dominant relaxation mechanisms for **1** and **2**, **3** and **4** respectively.

INTRODUCTION

Lanthanide-based coordination complexes have gained considerable attention in recent years owing to their unique physical and chemical properties that is not replicated by other metal ions in the entire periodic table.[1-4] Ever since the discovery of SMM behavior in the mononuclear $[TbPc_2]^-$ complex (Pc: phtalocyanine),[5] interest in Ln-based SMMs has been continuously growing in an unabated manner.[6-10] The inherently large single-ion anisotropy in lanthanide ions, owing to strong spin-orbit coupling (SOC) accompanied by a large spin ground state makes them particularly appealing in the field of molecular nanomagnetism.[6, 11, 12] Although crystal field effects in lanthanide complexes are much smaller, they have a subtle and important influence in determining and harnessing magnetic anisotropy in the molecular complex.[13-16] The strength of the crystal field dictates the magnitude of splitting in the ground $^{2S+1}L_J$ multiplet of the Ln(III) ions and therefore subtle changes in the crystal field/coordination geometry allows distinct dynamics of magnetic relaxation processes.[17-19]

Among the various lanthanide ions that have been investigated, Dy^{III} has received the maximum attention because of a relatively high *J* value of 15/2 and because it is a Kramer's ion.[19-22] The latter feature naturally leads to a bistable ground doublet state which is advantageous for observing SMM behavior. In addition, Dy^{III} possesses fewer β electrons in the 4f shell which renders adoption of a more anisotropic shape in the electron density under the influence of the electrostatic potential generated by the crystal field.[23] For such a system, a non-distorted disk shape where the electron density of the ligands are more concentrated above and below the plane of the disk would result in collinear magnetic moments in the ground state as well as up to several excited m_J states of the ground multiplet leading to a high energy barrier for magnetization reversal (U_{eff}).[24-27] Therefore, a two-coordinate linear

geometry is ideal to harness the magnetic anisotropy for such an ion.[25, 27, 28] But to stabilize the highly charged Ln(III) ions in such a geometry is extremely challenging and thus the focus has shifted to *pseudo*-linear complexes with strong ligands coordinated in the axial positions and weak ligands coordinated in the equatorial positions.[29-32] Utilizing this strategy many mononuclear non-organometallic complexes of the square antiprismatic and tetra-, penta-/hexagonal bipyramidal geometries around the Dy(III) ion were designed and found to be SMMs with various energy barriers of magnetization reversal.[32-35] Currently, the dinuclear dysprosium complex $[Dy_2(C_5{}^{i}Pr_5)_2(\mu\text{-}I)_3]$, which contains a $1e^-$ Dy–Dy bond, holds the record highest energy barrier of 2345 K and T_B of 72 K.[36]

In spite of considerable progress, fine tuning the magnetic properties of the Ln(III) ions via geometrical/microenvironment modifications is still a challenging task. We have been utilizing pentadentate hydrazone ligands (H_2L and H_4L) for some time to rationally design mononuclear pentagonal bipyramidal (PBP) Ln(III) complexes.[19, 37, 38] In earlier studies from our laboratory, we have used these ligands to synthesize mononuclear PBP Ln(III) complexes where the ligands provided a rigid equatorial pentagonal coordination while the axial sites were occupied by either two Cl^- ligands, two phosphine oxide ligands or by one chloride and one phosphine oxide ligands (Figure 1). We reported a detailed investigation of the single-ion magnetic behavior of several Ln(III) ions in this coordination environment. It was of interest to replace the Cl^- ligand with other anionic ligands to examine their influence on magnetic behaviour. We choose the ubiquitous carboxylate ligands for this purpose and have successfully synthesized a series of neutral mononuclear Dy(III) complexes, $[Dy(L)(Ph_3PO)(OOCR)]$ (where R = C_6H_5 (**1**), $C(CH_3)_3$ (**2**), CF_3 (**3**)). Further, we utilized an aromatic dicarboxylate ligand to synthesize a dinuclear complex, $[Dy_2(L)_2(Ph_3PO)_2\{(OOC)_2\}C_6H_4]$ (**4**) following the same synthetic strategy. The synthesis, structure, theoretical, and magnetic properties of **1**–**4** are reported herein.

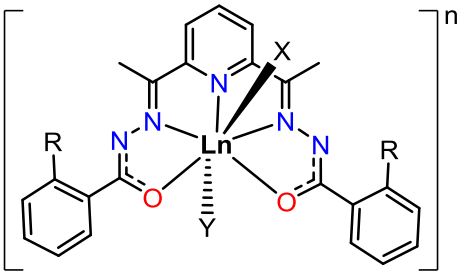

L′, R = OH ; Ln = Dy, Tb; X = Y = Cl ; n = 1–
L, R = H ; Ln = Dy; X = Y = Cy_3PO ; n = 1+
L, R = H ; Ln = Dy, Tb, Gd, Er; X = Cy_3PO, Y = Cl ; n = 0
L, R = H ; Ln = Dy; X = Ph_3PO, Y = Cl ; n = 0

Figure 1. Previously reported mononuclear PBP Ln(III) complexes derived from the H_4L/H_2L ligands.[37-39]

RESULTS AND DISCUSSION

Synthetic aspects. Rational design of mononuclear Ln(III) complexes utilizing multidentate and/or macrocyclic ligands has emerged as a promising synthetic strategy to engineer specific coordination geometry around the Ln(III) center.[30, 33, 40-43] The aim is to generate an axial crystal field for ions such as Dy(III) and Tb(III) which has been shown to help increase the Ising-type magnetic anisotropy and therefore beneficial for observing SMM properties. We have previously reported the synthesis of mononuclear heptacordinate and octacoordinated Ln(III) complexes using pentadentate chelating ligands which effectively provide a rigid equatorial plane.[37-39, 44] Recently, we reported the synthesis of a series of neutral mononuclear complexes, $[(L)Ln^{III}(R_3PO)Cl]$ (Ln = Dy Tb, Gd, Er when R = cyclohexyl; Ln = Dy when R = phenyl) where one axial site was occupied by a Cl^- ligand while a phosphine oxide ligand occupied the other axial site.[37] In these complexes, the Dy(III) analogues were found to be field-induced SMMs with a moderate energy barrier for magnetization reversal. It occurred to us that the replacement of the axial chloride by a carboxylate ligand would result in a change of the geometry around the lanthanide ion, while at the same time providing an opportunity to modify the crystal field subtly. Accordingly, we were able to isolate a new family of neutral

mononuclear Dy(III) complexes, [Dy(L)(Ph_3PO)(OOCR)] (where R = Ph (**1**), $C(CH_3)_3$ (**2**), CF_3 (**3**)) (Scheme 1). The planarity of the rigid pentadentate ligand, $[L]^{2-}$ allowed a smooth substitution of the axial chloride by the carboxylate without disturbing the geometry around Dy(III). Also, this methodology allowed us to vary the substituent on the carboxylate group quite readily. Further, a careful modulation of the reaction stoichiometry and the utilization of an aromatic dicarboxylate ligand resulted in a structurally analogous neutral dinuclear Dy(III) complex, $[Dy_2(L)_2(Ph_3PO)_2\{(OOC)_2\}C_6H_4]$ (**4**) (Scheme 2).

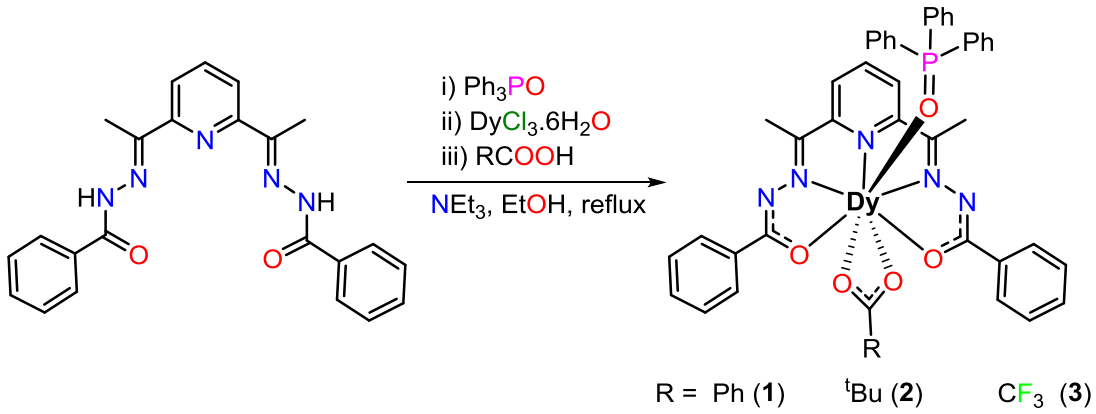

Scheme 1. Reaction scheme for the synthesis of **1**–**3**.

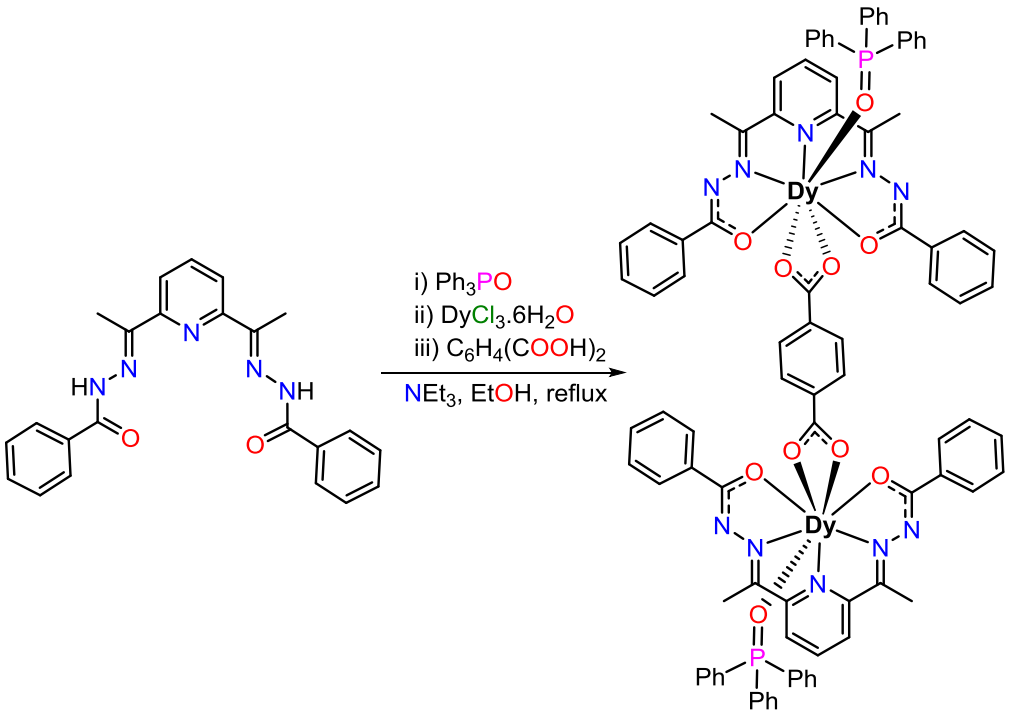

Scheme 2. Reaction scheme for the synthesis of **4**.

X-ray Crystallography

The complexes **1** and **2** crystallize in the monoclinic crystal system in the $P2_1/n$ and Cc space groups respectively whereas **3** and **4** crystallize in the triclinic crystal system in the P-1 space group. The crystallographic data and refinement parameters of all the complexes are given in Table 2. All the complexes are eight-coordinate because of the aniso-bidentate coordination behavior of the carboxylate ligands. The overall molecular structure of complexes **1**–**4** is essentially identical although complex **4** is a bimetallic complex. The molecular structures **1** and **4** are shown in Figures **2** and **3**, while those of **2** and **3** are given in the Electronic Supporting Information (ESI) (Figures S1 and S2). In view of the structural similarities present in the complexes, we discuss below the molecular structures of complexes **1** and **4**.

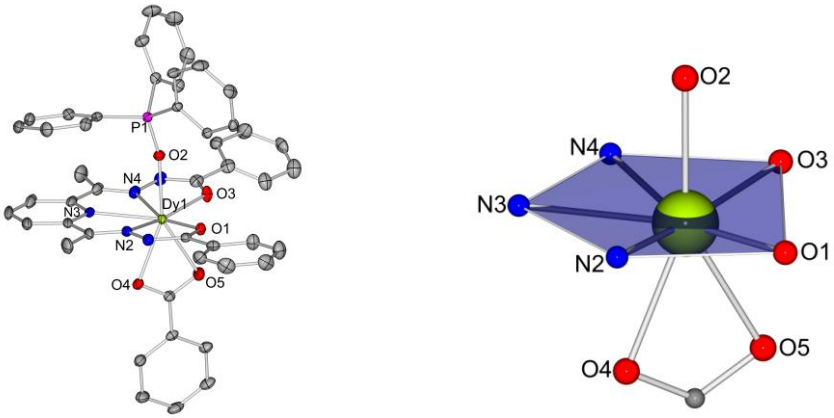

Figure 2. Molecular structure of complex **1**. Thermal ellipsoids at 30% probability level are shown (*left*) and the immediate coordination geometry around the Dy1 center (*right*). (The H atoms, disordered atoms and the masked solvent molecules are omitted for clarity)

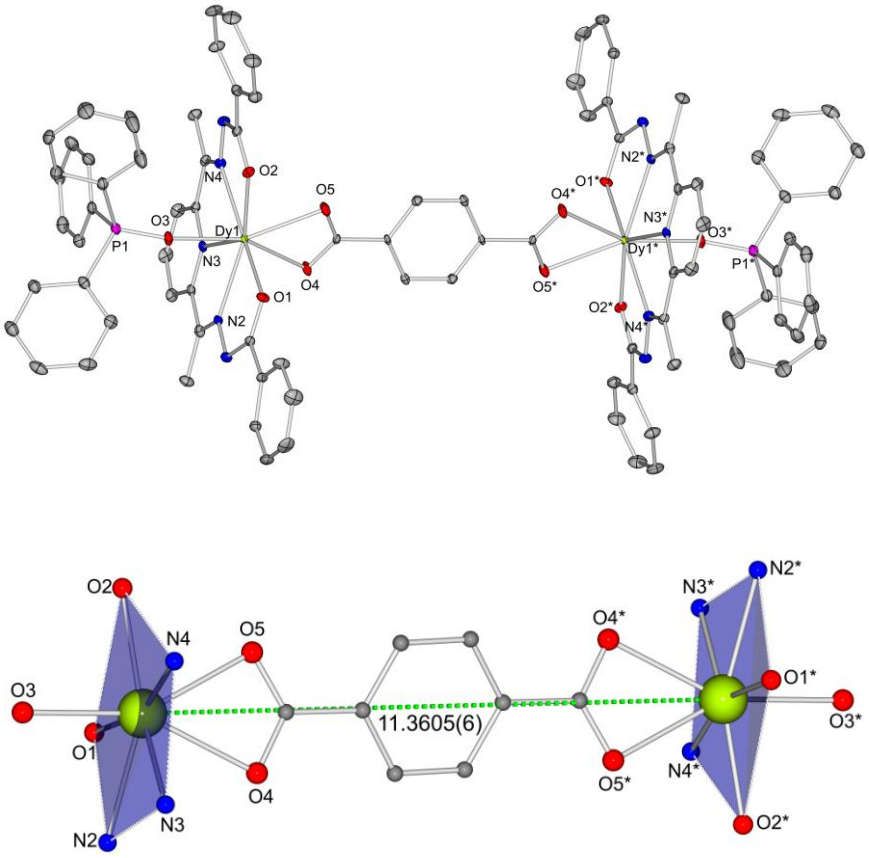

Figure 3. Molecular structure of complex **4**. Thermal ellipsoids at 30% probability level are shown (*top*) and the immediate coordination geometries around the Dy centers (*bottom*). (The H atoms are omitted for clarity)

The complexes are formed by the coordination action of a dianionic pentadentate ligand $[L]^{2-}$, one Ph_3PO and a benzoate ligand leading to the eight-coordinate Dy(III) centers (Figure 2). The equatorial positions comprise of a *pyridyl* N atom (N3), two *imino* N atoms (N2 and N4), and two *enolate* O atoms (O1 and O3). The equatorial plane of the complexes consists of four *five*-membered rings. A Ph_3PO ligand coordinates axially to the Dy(III) center above the pentagonal plane. Finally, the benzoate ligand coordinates to the Dy(III) center below the pentagonal plane in an anisobidenate κ^2O chelating mode and completes the coordination sphere around the metal ion. It is worth emphasizing that the overall structural features of **4** (see Figure 3) is essentially similar to **1** except that it is a dinuclear complex which is formed as a result of the bridging coordination of the terephthalate ligand. The average enolate and

imino bond lengths of $[L]^{2-}$ in **1–4** and the previously reported complexes are given in Table S1(see ESI). In all the complexes, the C=N bond distances are in the range 1.272(15)–1.338(15) Å and the C–O bond distances are in the range 1.280(3)–1.303(15) Å which are quite comparable with the previously reported complexes. Further, the Dy−O_{phos} bond distances in **1**–**4** are slightly longer than the previously reported complexes (see Table S1).

The average equatorial Dy–O/N bond distances are 2.297(2)/2.483(2) Å in the case of **1** whereas the average equatorial Dy–O/N bond distances for **4** are 2.298(3)/2.474(3) Å (see Table 1 for **1** and S3 for **4**). The average Dy−$O_{carboxy}$ bond distance is 2.4063(17) Å for **1** and 2.430(3) Å for **4**. The O_{phos}−Dy−$O_{carboxy}$ bond angles are 150.02(6)° and 156.23(6)° for **1** whereas in the case of **4**, the bond angles are 152.26(11)° and 154.20(10)°. The intramolecular Dy· · · Dy distance in the complex **4** is 11.360(7) Å (Figure 3 (bottom)). The actual coordination environment of the Dy(III) ions in **1**–**4** were analyzed with Continuous-Shape Measures using the SHAPE program and the results are given in Table S2.[45, 46] It reveals comparable coordination geometries between the distorted triangular dodecahedron (D_{2d}) and the distorted biaugmented trigonal prism (C_{2v}) geometries (Figures S3-S6). Selected bond distances and angle parameters of **1** are tabulated in Table 1 whereas for **2**−**4** it is given in Table S3 (see ESI).

Table 1. Bond distance and bond angle parameters of complex **1**.

Bond distances (Å)		**Bond angles (°)**			
		O3−Dy1−O5	73.56(7)	O3−Dy1−O4	119.37(6)
		O3−Dy1−N4	64.58(6)	O3−Dy1−N3	127.25(7)
		O3−Dy1−N2	159.92(6)	O1−Dy1−O3	100.62(6)
Dy1−O3	2.300(2)	O1−Dy1−O5	82.23(7)	O1−Dy1−O4	99.62(6)
Dy1−O1	2.294(2)	O1−Dy1−N4	162.59(6)	O1−Dy1−N3	128.35(6)
Dy1−O2	2.280(2)	O1−Dy1−N2	64.38(6)	O2−Dy1−O3	81.39(6)

Dy1−O5	2.418(2)	O2−Dy1−O1	86.56(6)	O2−Dy1−O5	150.02(6)
Dy1−O4	2.394(2)	O2−Dy1−O4	156.23(6)	O2−Dy1−N4	82.27(6)
Dy1−N4	2.481(2)	O2−Dy1−N3	83.15(6)	O2−Dy1−N2	84.29(6)
Dy1−N3	2.491(2)	O5−Dy1−N4	101.01(8)	O5−Dy1−N3	125.25(6)
Dy1−N2	2.478(2)	O5−Dy1−N2	114.98(7)	O4−Dy1−O5	53.67(6)
		O4−Dy1−N4	95.93(6)	O4−Dy1−N3	75.00(6)
		O4−Dy1−N2	77.95(6)	N4−Dy1−N3	63.51(7)
		N2−Dy1−N4	127.19(7)	N2−Dy1−N3	64.29(7)

The solid-state structures of all the complexes show dominant π···π stacking interactions in combination with C–H/π interactions (Tables S4-S11).[47, 48] Complexes **1**, **2** and **4** show intramolecular π···π stacking interactions between the pyridyl ring of the $[L]^{2-}$ ligand and one of the phenyl rings of Ph_3PO ligand with centroid-centroid distance of $d_{Cg1\cdots Cg7}$ = 3.8201(15) Å, $d_{Cg1\cdots Cg6}$ = 3.565(10) Å and $d_{Cg1\cdots Cg6}$ = 3.821(3) Å respectively (see Figure 4(a) for **1** and Figures S8 (for **2**) and S12 (for **4**)). Again, the pyridyl ring of the $[L]^{2-}$ ligand in the case of complex **1** is involved in intermolecular π···π stacking interaction ($d_{Cg1\cdots Cg8}$ = 4.6757(15)Å) with one of the phenyl rings of the Ph_3PO ligand assisting in the formation of a one-dimensional (1D) supramolecular chain (Figure 4(b)). On the other hand, the pyridyl ring in the case of complexes **3** and **4** are involved in intermolecular π···π stacking interaction with one of the phenyl rings of the $[L]^{2-}$ ligand leading to dimeric ($d_{Cg1\cdots Cg3}$ = 4.238(2) Å) and polymeric ($d_{Cg1\cdots Cg2}$ = 4.251(3) Å) structures respectively (Figures S10 (*left*) and S13 (*top*)). In addition, one of the phenyl rings of Ph_3PO ligand in complex **3** is involved in intermolecular π···π stacking interaction ($d_{Cg6\cdots Cg6}$ = 3.673(2) Å) leading to a dimeric structure (Figure S10 (*right*)) whereas one of the phenyl rings of the $[L]^{2-}$ ligand in complex **4** is involved in intermolecular π···π stacking interaction ($d_{Cg3\cdots Cg3}$ = 4.849(3) Å) to form a one-

dimensional (1D) supramolecular chain along the crystallographic ***c*** axis (Figure S13 (*bottom*)). Interestingly, the presence of a terminal phenyl ring in complex **1**, results in a large offset π···π stacking interaction ($d_{Cg5\cdots Cg5}$ = 4.9925(16) Å) which leads to a dimeric structure (Figure 4(c)). In addition to the π···π stacking interactions, all the complexes show numerous tilted-T-shaped C–H/π interactions. In complex **1**, four different intermolecular C–H/π interactions were observed with H···Centroid distance in the range 2.63 Å–3.00 Å and C···Centroid distance in the range 3.473(3) Å–3.835(3) Å (Figure S7). Complex **2** shows three different intermolecular C–H/π interactions with H···Centroid distance in the range 2.59 Å–2.98 Å and C···Centroid distance in the range 3.28(2) Å–3.819(17) Å (Figure S9). Complex **3** shows only one intermolecular C–H/π interaction between one of the H's of the CH_3 groups and the one of the phenyl rings of the $[L]^{2-}$ ligand to form a one-dimensional (1D) supramolecular chain along the crystallographic ***b*** axis with H···Centroid distance of 2.86 Å and C···Centroid distance of 3.555(4) Å (Figure S11). Finally, complex **4** show one intramolecular C–H/π interaction ($d_{H30\cdots Cg3}$ = 2.84 Å and $d_{C\cdots Cg}$ = 3.546(8) Å) and three different intermolecular C–H/π interactions with H···Centroid distance in the range 2.57 Å–2.83 Å and C···Centroid distance in the range 3.495(6) Å–3.661(6) Å (Figures S14 and S15).

(a) (c)

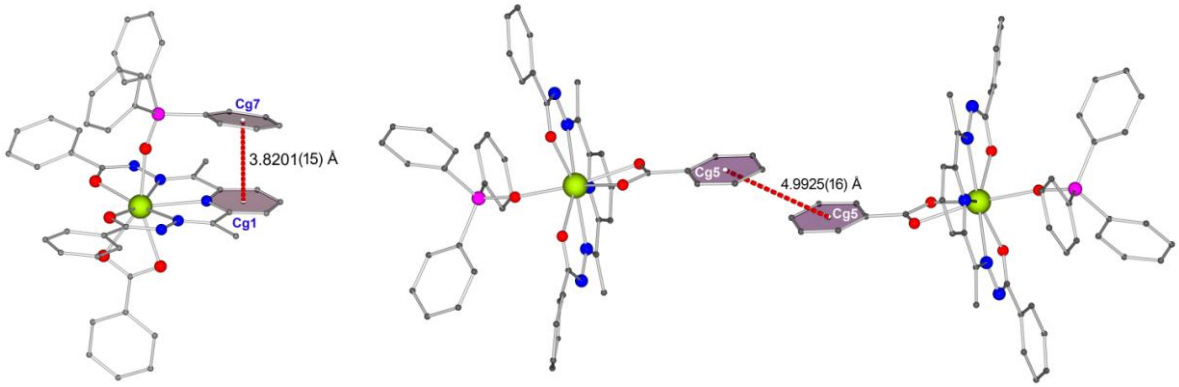

(b)

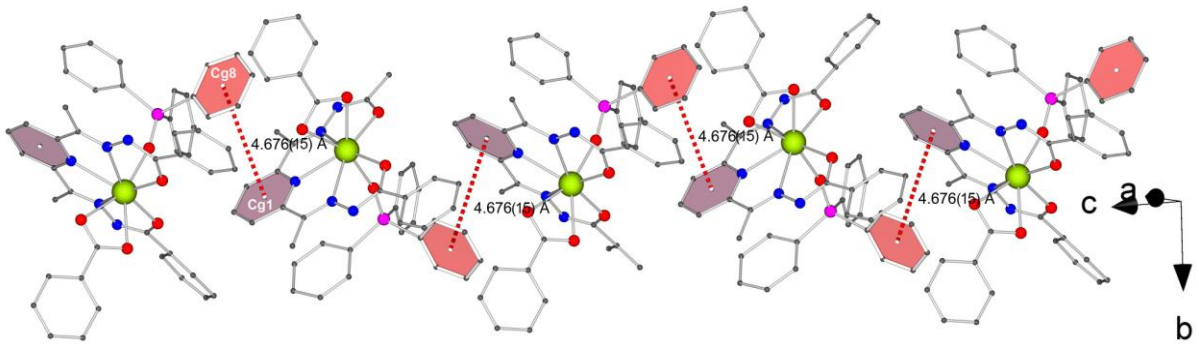

Figure 4. Illustrations of intra-/intermolecular π···π ($d_{Cg1\cdots Cg7}$ = 3.8201(15) Å, $d_{Cg1\cdots Cg8}$ = 4.676(15) Å and $d_{Cg5\cdots Cg5}$ = 4.9925(16) Å) stacking interactions present in complex **1** (H-atoms are omitted for clarity).

The packing diagrams of **1**–**4** were analyzed to measure the shortest intermolecular Dy· · · Dy distances. The mononuclear complexes **1**–**3** show intermolecular Dy· · · Dy distances of 9.0013(6) Å, 9.1961(10) Å and 8.0821(5) Å respectively while the binuclear complex **4** shows the shortest distance of 10.2273(4) Å (see Figures S16–S18).

Magnetic Properties

Magnetic measurements as a function of temperature were performed on polycrystalline samples in the temperature range of 1.8-300 K and a static magnetic field of 0.5 T. The χT values at room temperature (14.20, 14.01, 14.00 and 27.85 emu·K·mol^{-1} for **1**, **2**, **3** and **4** respectively) are in good agreement with the expected value for Dy(III) (S = 5/2, L = 5, $^6H_{15/2}$, g = 4/3, C = 14.17 emu·K·mol^{-1}) mono and dinuclear complexes. Upon cooling, the χT product decreases, because of thermal depopulation of the low-lying crystal-field states (Figure 5(*left*)).

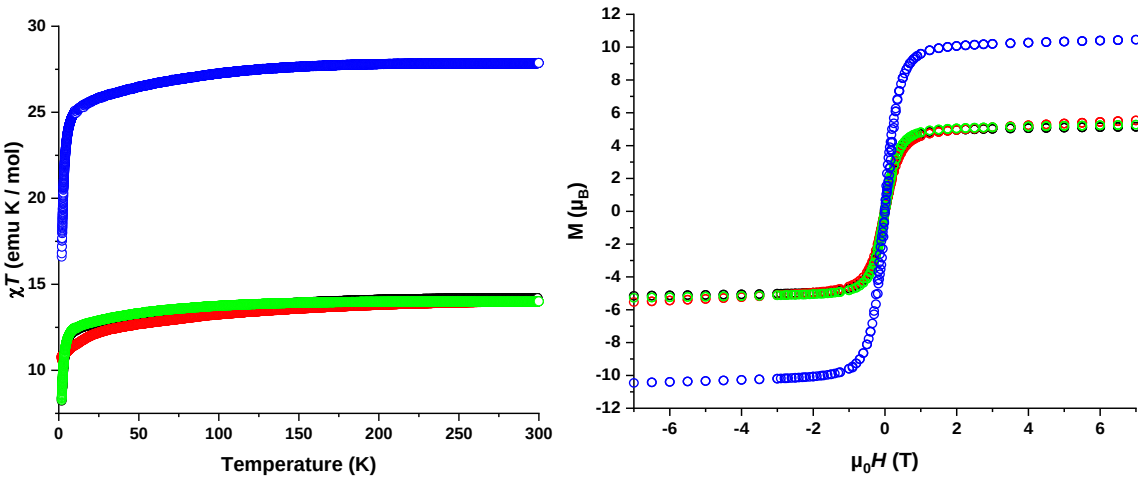

Figure 5. χT = f(T) under a static magnetic field of 0.5 T (left) and M = f($\mu_0 H$) at 1.8 K (right) for compounds **1** (black), **2** (red), **3** (green) and **4** (blue).

The field-dependent magnetizations at low temperature present a rapid increase at low fields and reaches an almost constant value above 2 T (5.15, 5.53, 5.27 and 10.46 μ_B at 7 T and 1.8 K for **1**, **2**, **3** and **4** respectively).

AC susceptibility measurements as a function of the AC field frequency with and without applied DC field were further performed in order to study the dynamics of the relaxation of magnetization at low temperatures.

Despite their similar structure, all four complexes present a different dynamic behaviour. For **1**, AC susceptibility measurements as a function of the AC field frequency performed under zero DC field are presented in Figure 6.

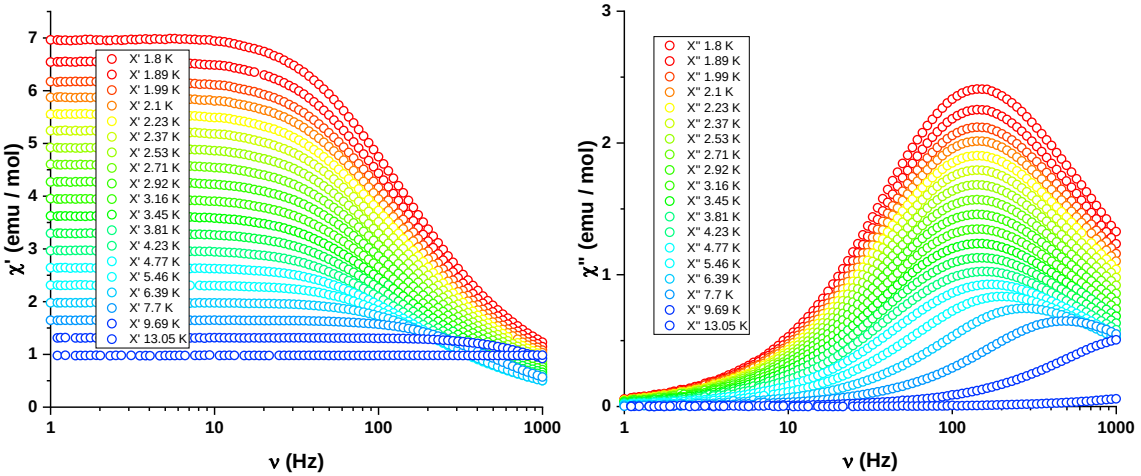

Figure 6. In-phase (left) and out-of-phase (right) susceptibility curves for complex **1** with an AC field of 2 Oe under a static DC field of 0 Oe at various temperatures.

The low-temperature frequency-dependent AC susceptibility data were further analyzed by using a generalized Debye model to fit the Cole–Cole plots (Figure S19 and Table S12 in ESI). The temperature dependence of the relaxation time can be fitted considering Quantum Tunneling and Orbach mechanisms ($\tau^{-1} = \tau_0^{-1} \cdot \exp(-\Delta/T) + \tau_{QTM}^{-1}$) leading to $\tau_0 = 2.7(6) \times 10^{-6}$ s, $\Delta = 39$ (2) K and $\tau_{QTM} = 1.00(1) \times 10^{-3}$ s, or, with equal fit quality, considering Quantum Tunneling and Raman mechanisms ($\tau^{-1} = CT^n + \tau_{QTM}^{-1}$) leading to $C = 0.19(7)$ $s^{-1}K^{-5.1}$, $n = 5.1(1)$ and $\tau_{QTM} = 1.01(1) \times 10^{-3}$ s (Figure 7).

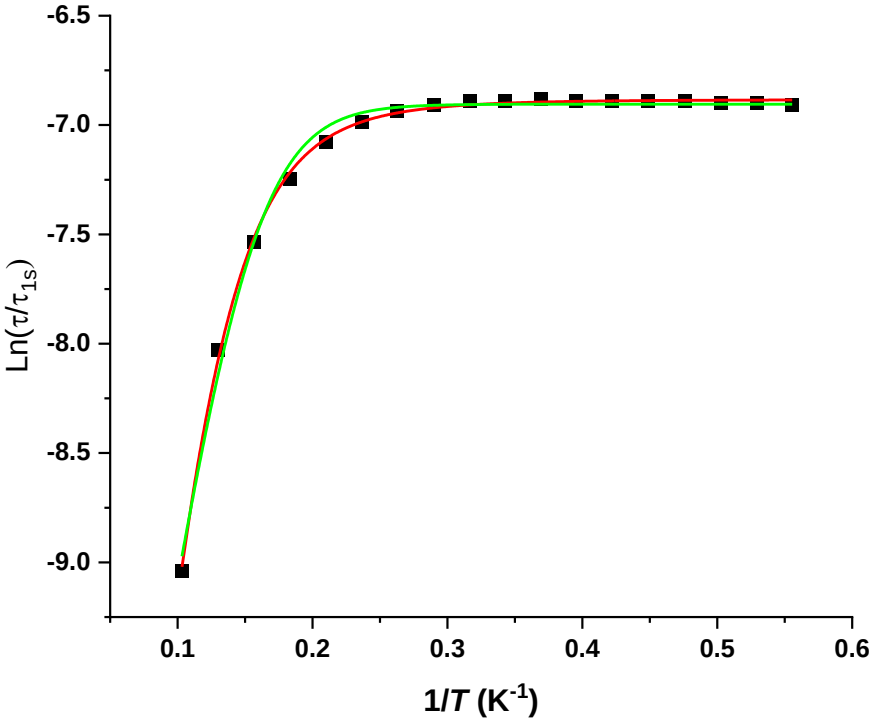

Figure 7. Relaxation time (represented as $Ln(\tau/\tau_{1s})$, with τ_{1s} = 1 s) as a function of 1/T for **1** under a static DC field of 0 Oe (full squares: experimental points, full green line: best fit considering QTM and Orbach mechanisms, full red line: best fit considering QTM and Raman mechanisms (see text)).

For **2**, AC susceptibility measurements as a function of the AC field frequency under 0 DC field show a frequency dependence with two mechanisms or relaxation times visible. Moreover, the frequencies of the observed maxima in the $\chi''(\nu)$ seem to be almost independent of the temperature, indicating a relaxation mechanism dominated by Quantum Tunneling (Figure S20 in SI). In order to reduce QTM, AC susceptibility measurements were then performed as a function of the AC field frequency under a DC field of 500 Oe (see ESI for the determination of this optimized DC field) (Figure 8).

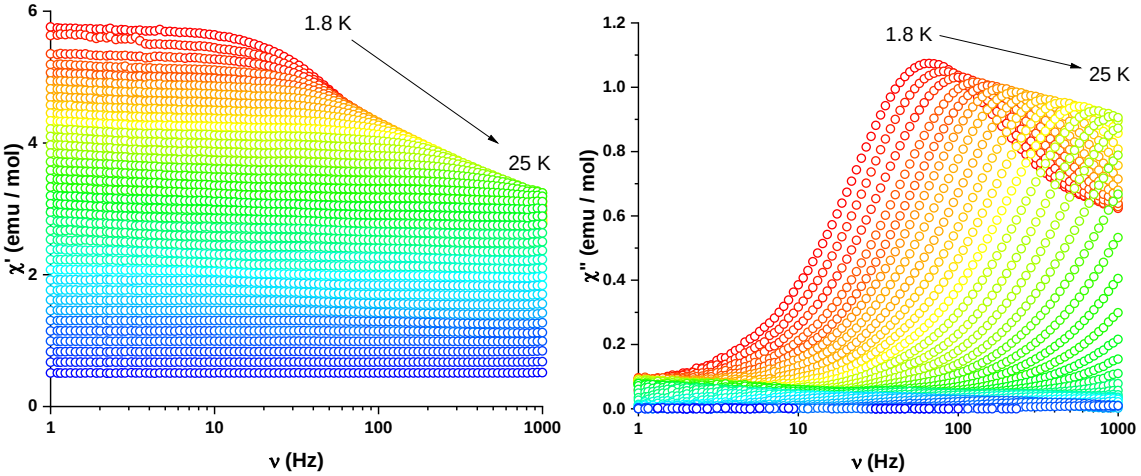

Figure 8. In-phase (left) and out-of-phase (right) susceptibility curves for complex **2** with an ac field of 2 Oe under a static DC field of 500 Oe at various temperatures.

The evolution of the relaxation times can be fitted by an Arrhenius law, leading to $\tau_0 = 3.9(3)\times10^{-7}$ s and an effective energy barrier $\Delta = 15.8(2)$ K, about half than for **1** (Figure 9).

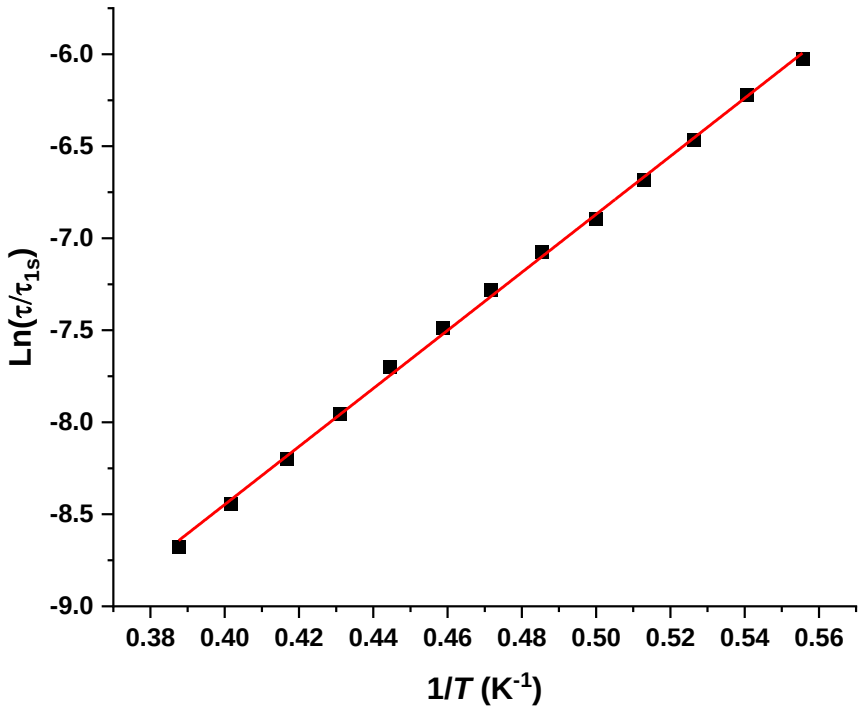

Figure 9. Relaxation time (represented as $Ln(\tau/\tau_{1s})$, with τ_{1s} = 1 s) as a function of 1/T for **2** under a static DC field of 500 Oe (full squares: experimental points, full line: best fit (see text)).

For **3**, AC susceptibility measurements as a function of the AC field frequency under 0 DC field show a frequency dependence with but without maximum in the frequency range available (see SI). In order to reduce QTM, AC susceptibility measurements were then performed as a function of the AC field frequency under a DC field of 1000 Oe (see SI for the determination of this optimized DC field) (Figure 10).

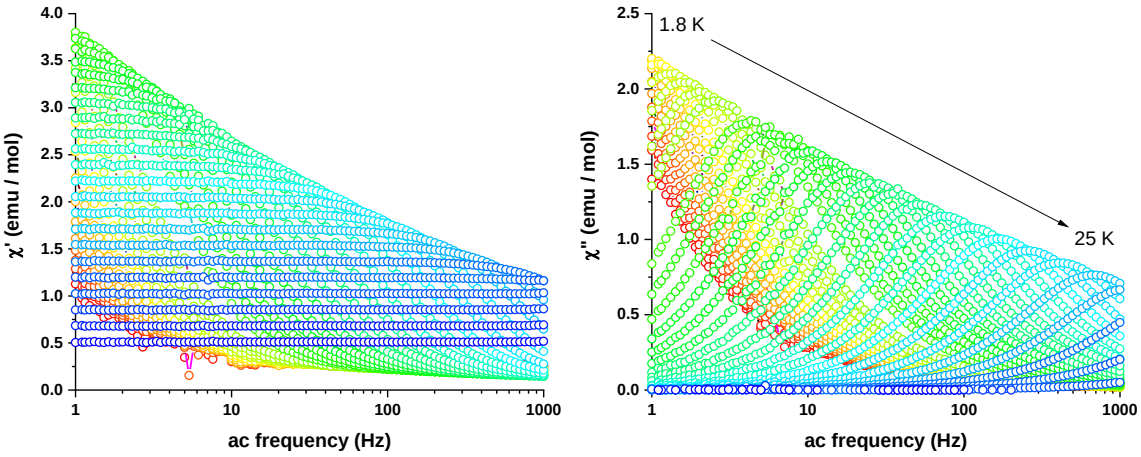

Figure 10. In-phase (left) and out-of-phase (right) susceptibility curves for complex **3** with an AC field of 2 Oe under a static DC field of 1000 Oe at various temperatures.

The temperature evolution of the relaxation time is well fitted by a Raman relaxation process, $\tau^{-1} = C \times T^{n}$, leading C = 0.031(2) $s^{-1} \cdot K^{-6.1}$ and n = 6.1(1) (Figure 11).

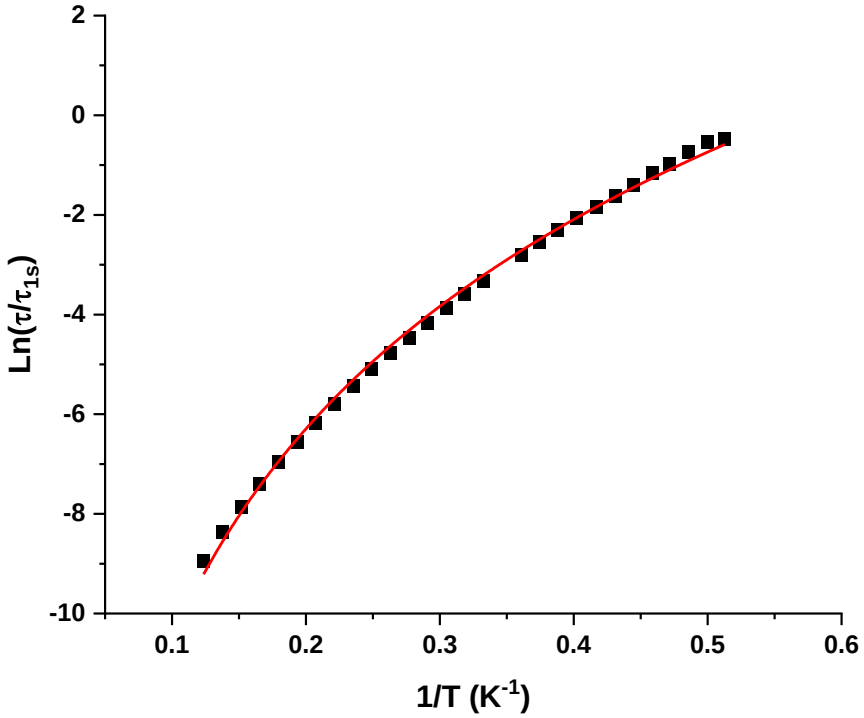

Figure 11. Relaxation time (represented as $Ln(\tau/\tau_{1s})$, with τ_{1s} = 1 s) as a function of 1/T for **3** under a static DC field of 1000 Oe (full squares: experimental points, full line: best fit (see text)).

Finally, for **4**, AC susceptibility measurements as a function of the AC field frequency performed under 0 DC field are presented in Figure 12.

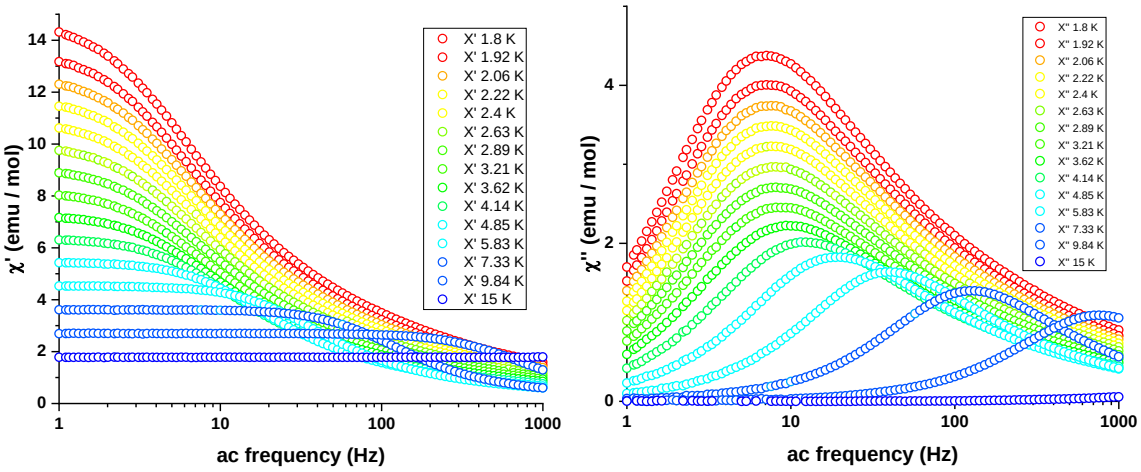

Figure 12. In-phase (left) and out-of-phase (right) susceptibility curves for complex **4** with an AC field of 2 Oe under a static DC field of 0 Oe at various temperatures.

The temperature dependence of the relaxation time can be fitted considering Quantum Tunneling and Raman mechanisms ($\tau^{-1} = CT^{n} + \tau_{QTM}^{-1}$) leading to C = 0.0067(7) $s^{-1}K^{-5.8}$, n = 5.8(1) and τ_{QTM} = 2.15(3)×10^{-2} s (Figure 13).

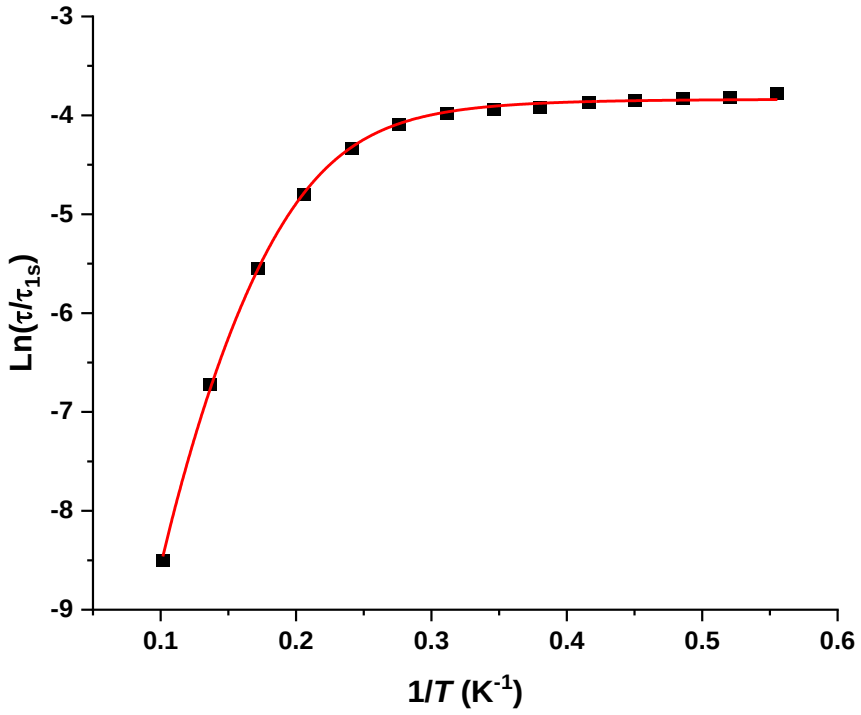

Figure 13. Relaxation time (represented as Ln(τ/τ_{1s}), with τ_{1s} = 1 s) as a function of 1/T for **4** under a static DC field of 0 Oe (full squares: experimental points, full line: best fit (see text)).

The comparison of the relaxation parameters for compounds **1**-**4** is given in Table 2 below.

Table 2. Comparison of the relaxation parameters for compounds **1**-**4**

Compound	**1**	**2**	**3**	**4**
DC field (Oe)	0	500	1000	0
Relaxation mechanism	QTM + Orbach or QTM + Raman	Orbach	Raman	QTM + Raman
Parameters	τ_{QTM} = 1.00(1)×10^{-3} s τ_0 = 2.7(6)×10^{-6} s Δ = 39 (2) K or	τ_0 = 3.9(3)×10^{-7} s Δ = 15.8(2) K	C = 0.031(2) $s^{-1}\cdot K^{-6.1}$ n = 6.1(1)	τ_{QTM} = 2.15(3)×10^{-2} s C = 0.0067(7) $s^{-1}K^{-5.8}$ n = 5.8(1)

	τ_{QTM} = 1.01(1)×10^{-3} s C = 0.19(7) $s^{-1}K^{-5.1}$ n = 5.1(1)			

Theoretical Studies

To shed light on the origin of magnetic anisotropy and magnetic relaxation in complexes **1**-**4**, we have carried out complete active space self-consistent field (CASSCF) calculations on the hydrogen-optimized X-ray crystal structures. CASSCF/SINGLE_ANISO methodology has been very robust in analyzing the electronic and magnetic properties of lanthanide-based complexes.[49, 50] In complexes **1**-**3**, the Dy(III) ion possesses a distorted pentagonal bipyramidal geometry with the following molecular formula [Dy(L)(Ph_3PO)(OOCR)] (where R = C_6H_5 (**1**), $C(CH_3)_3$ (**2**), CF_3 (**3**)), where main structural differences arise due to the different -R groups. CASSCF computed energy span of the low-lying 21 sextets are ~35159, ~35145 and ~35307 cm^{-1} for complexes **1**-**3**, respectively. The inclusion of the spin-orbit coupling via RASSI-SO mixing yields the SOC spectrum, and the energy span of low-lying eight Kramers doublets (KDs) corresponding to $^6H_{15/2}$ ground state are 522.2, 519.8 and 545.7 cm^{-1} for complexes **1**-**3**, respectively (see Tables S18-S20). Interestingly, the computed ground state g-values are highly axial for complexes **1** and **2** (g_{xx} = 0.024, g_{yy} = 0.132 and g_{zz} = 19.328 for **1**; g_{xx} = 0.039, g_{yy} = 0.098 and g_{zz} = 19.110 for **2**), with a sizable transverse component in g-values of **3** (g_{xx} = 0.904, g_{yy} = 4.999 and g_{zz} = 15.4227). In complexes **1** and **2**, wavefunction decomposition predicts the stabilization of $^6H_{15/2}$ as the ground state KD; however, it lacks pure Ising type (g_{xx} = g_{yy} = 0) ground state. For complex **3**, we noticed stabilization of m_J $|\pm15/2\rangle$ primarily as the ground state, which is heavily mixed with the other excited m_J $|\pm11/2\rangle$ and $|\pm7/2\rangle$ states [56.7% $|\pm15/2\rangle$ + 24.6% $|\pm11/2\rangle$ + 7.4% $|\pm7/2\rangle$] states (Table S25). CASSCF computed beta spin density does not show a typical disk-type

feature corresponding to pure m_J |±15/2⟩ ground state, indicating the ground state is heavily mixed with other excited KDs. The computed beta spin density of complexes **1-2** differs from complex **3** due to the differences in the local coordination environment. The main magnetic axis (g_{zz}) of the ground state KD is located in the equatorial plane and passes through one of the O atoms of the L ligand by making angles of 19.4°, 12.3° and 24.0° in complexes **1-3**, respectively. The observed orientation of the g_{zz} axis in complexes **1-3** matches well with the previously studied Dy(III) ion in the PBP geometry.[37, 38] In complexes **1-3**, the first excited KD is majorly m_J |±13/2⟩ in nature, which is significantly mixed with other excited KDs, resulting in sizable transverse g-values (g_{xx} = 0.941, g_{yy} = 1.780 and g_{zz} = 17.591 for **1**; g_{xx} = 0.138, g_{yy} = 0.235 and g_{zz} = 19.038 for **2** and g_{xx} = 1.260, g_{yy} = 2.154 and g_{zz} = 10.692 for **3**) (see Table 3). The energy of the first excited KD is located at 77.3, 51.5 and 29.3 cm^{-1} above the ground state KD for complexes **1-3**, respectively (see Table S18-S20). Alongside, we have noticed that the orientation of g_{zz} axis of the first excited KD is tilted by 123.1°, 39.8° and 4.8° from the ground state g_{zz} orientation, which ensures the thermal assisted magnetic relaxation via the first excited KDs. This indicates that the differences in the magnetic properties are essentially due to the differences in the axial ligand fields. In addition to this, we have also computed the *ab initio* blockade barrier for magnetic relaxation for complexes **1-3**, by computing the transverse magnetic moments between the KDs. The computed transverse magnetic moments between the ground state KDs are 2.2 $x10^{-2}$, 2.3 $x10^{-3}$ and 9.8 $x10^{-1}\mu_B$, respectively, for complexes **1-3**, suggesting fast QTM for **3** compared to complexes **1** and **2**. On the other hand, the transverse magnetic moment connecting the ground and the first excited KDs is always an order higher than the ground connecting doublets, which predicts the thermal-assisted quantum tunneling of magnetization (TA-QTM) via the first excited KD to be dominant magnetic relaxation pathway. The small energy gap between the ground and first excited KD and significantly large ground state QTM diminish the zero-field

SMM behaviour in complexes **1-3**. Moreover, the computed SH parameters nicely reproduce the experimental static d.c. magnetic susceptibility data, which highlights the goodness of the computed data (see Figure S26 of ESI).

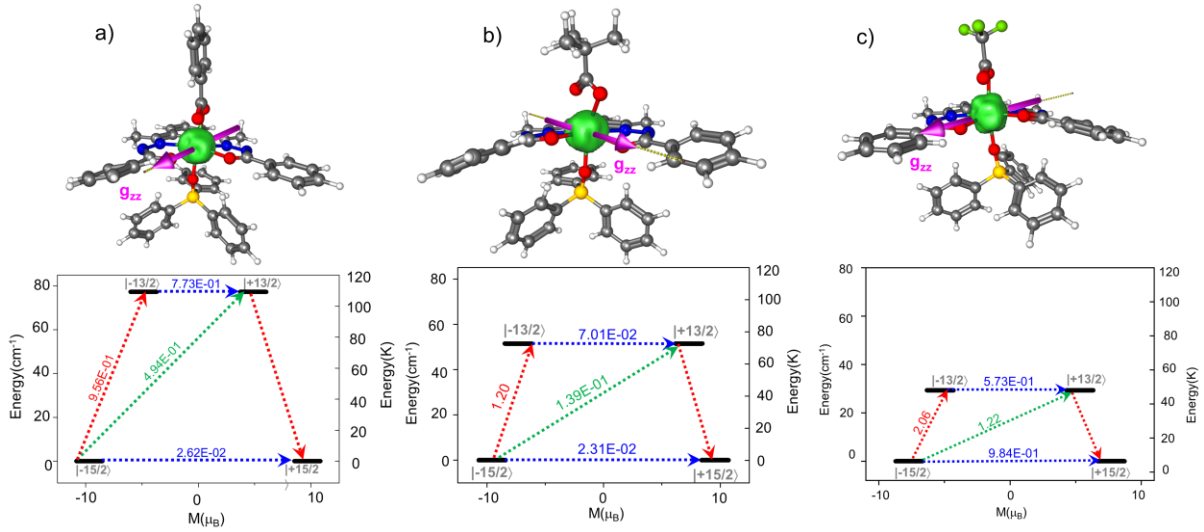

Figure 14. CASSCF/SINGLE_ANISO computed orientation of the main magnetization axes (g_{zz}) along with the beta-spin density and corresponding ab initio blockade barrier for complex a) **1**, b) **2** and c) **3**. The blue, red and green dotted lines represent the possible QTM, Orbach and Raman relaxations. CASSCF computed beta-spin density surface constructed with an iso-value of 0.0012 e^{-}/bohr^3. Color code: Green (Dy), red (O), blue (N), yellow (P), grey (C), and white (H).

Table 3: SINGLE_ANISO computed energies of the ground and first excited KDs corresponding g-

Complex	KDs	g_{xx}	g_{yy}	g_{zz}	Θ(°)	K_{QTM}	K_{QTM} (Exp)	U_{eff}	U_{cal}
1	KD1	0.0247	0.1323	19.3280	-	2.62E-02	1.00(1)E-03	30(32.5)	77.3

values, K_{QTM} values and Ucal values for complexes **1-4** along with experimental data.

	KD2	0.9410	1.7807	17.5915	123.1	7.73E-01			
2	KD1	0.0396	0.0987	19.1108	-	2.31E-02		12.1(13.6)	51.5
	KD2	0.1385	0.2350	19.0386	39.8	7.01E-02			
3	KD1	0.9045	4.9990	15.4227	-	9.84E-01		-	29.3
	KD2	1.2604	2.1540	10.6922	4.8	5.73E-01			
4 (Dy1)	KD1	0.0269	0.2055	18.9596	-	3.86E-02	2.15(3)E-02	-	19.2
	KD2	0.0456	0.2451	19.1090	144.3	5.43E-02			
4 (Dy2)	KD1	0.0267	0.2054	18.9553		3.86E-02	2.15(3)E-02	-	19.2
	KD2	0.0457	0.2450	19.1044	144.3	5.43E-02			

In complexes **1**-**3** with the general formula [Dy(L)(Ph_3PO)(OOCR)] (where R = C_6H_5 (**1**), $C(CH_3)_3$ (**2**), CF_3 (**3**)), the computed U_{cal} value changes with the change in the -R group. To understand the role of the -R group on magnetic anisotropy and magnetic relaxation, we have carefully analysed the structural and electronic effects associated with axial and equatorial ligands. Due to a similar equatorial ligand field (L), the ligand field effect from the equatorial plane is expected to be the same in all three complexes. For complexes **1** and **2**, the average axial/average equatorial bond ratio is <1 (0.98) compared to **3,** where the ratio is marginally >1, indicating structural topology favours the axial field in complexes **1** and **2** (see Table S16). On the other hand, the average axial/equatorial Loprop charges ratio is >1 for all the complexes **1**-**3**, indicating a favourable electrostatic environment to stabilize the m_J ±15/2 ground state in Dy(III) ion (see Table S17 and Figure S27). The close inspection of the Loprop charge analysis suggests the presence of hefty negative charges on the coordinated O atom of the R group in complex **1** (-0.730m) and **2** (-0.733) compared to complex **3** (-0.654), generating stronger axial ligand field for complexes **1**-**2**(see Figure S27). This arises due to the electron-withdrawing nature of the -CF_3 group in **3,** resulting in smaller charges on coordinated O atoms compared to -C_6H_5 (**1**), -$C(CH_3)_3$ (**2**) groups. Thus, the strong -I effect offered by the CF_3 group is the key to smaller barrier height in **3**, compared to complexes **1** and **2**. The analysis of computed crystal-field parameters B_k^q for complexes **1**-**3** show a considerable negative value of the axial B_2^0 parameter, indicating stabilization of the highest

m_J as the ground state. Moreover, the presence of significant and competing non-axial $B_2^{q=2,4,6}$ parameter clearly indicates the non-negligible magnetic anisotropy in the ground state (see Table S22). In addition, we have also observed that the barrier height in complexes **1-3** is much smaller than the previously reported [$L_{eq}DyL_{ax2}$] (where L_{ax} = Cl, Cy_3PO, Ph_3PO, L_{eq} = pentadentate ligand) complexes with similar ligand scaffolds, where U_{cal} values are ranging around 200 cm^{-1}.[37, 38] The presence of the (OOCR) group with bidentate η^2 coordinating ability distinguishes complexes **1-3** from previously reported complexes from a structural standpoint. Although the OOCR groups are strongly anionic in nature compared to the previously reported complexes with neutral Cy_3PO/PPh_3PO ligands, the presence of two -O atoms (η^2-mode) away from the z-axis (large cone/bite angle) contributes more towards the equatorial ligand field which is the main factor for drastically small barrier height in these complexes.[51, 52]

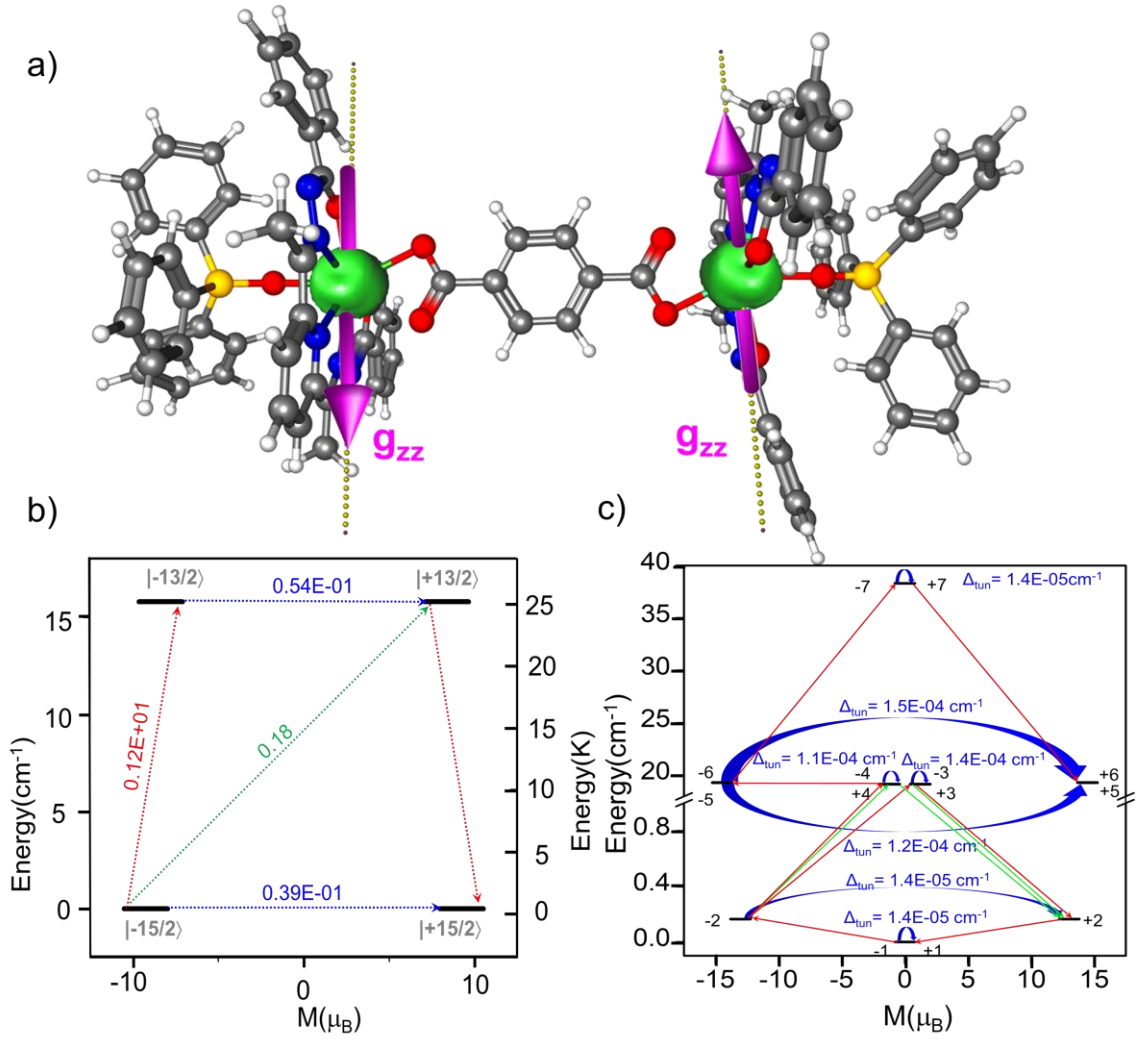

Figure 15. a) CASSCF/SINGLE_ANISO computed orientation of the main magnetization axes along with the beta-spin density for **4**; b) SINGLE_ANISO computed ab initio blockade barrier of **4**. c) POLY_ANISO extracted magnetic relaxation pathway between the exchange states of **4**. The blue, red and green lines represent the possible QTM, Orbach and Raman relaxations. Color code: Green (Dy), red (O), blue (N), yellow (P), grey (C), and white (H).

Complex **4** is a dimeric form of the **1**, where both the Dy(III) centers are bridged through a terephthalate ligand with Dy….Dy bond distance of 11.360 Å. In complex **4**, the computed energy span of eight low-lying KDs is 529.9 (529.8) cm^{-1} for Dy1(Dy2) centers, which is similar to what we observed in **1** (see Table S21). For individual Dy(III) ions of complex **4**, the computed g-values are highly axial in nature (g_{xx} = 0.0269, g_{yy} = 0.2055 and g_{zz} = 18.9596) for Dy1; (g_{xx} = 0.0267, g_{yy} = 0.2054 and g_{zz} = 18.9553) for Dy2), representing

predominant stabilization of the m_J ±15/2 as the ground state. For both the Dy1 and Dy2 centers, the computed g_{zz} axis state KD is located in the equatorial plane and arranged in an antiparallel fashion to each other. Although the structural and Loprop charge analysis indicates stabilization of the axial ligand field, the differences in the observed SOC spectrum arise due to local distortions. In complex **4**, the large bite angle (121.2^{o}) of the OOCR group in Dy1 and Dy2, along with a relatively long Dy-O1/Dy-O2 bond distance OOCR group compared to **1**, indicates a weak ligand field around the Dy(III) centers responsible small gap between the ground and first excited KD in **4** (Table S16 and Figure S30). The single-ion magnetic anisotropy analysis predicts a U_{cal} value of 19.2 cm^{-1} in complex **4**, 4x times smaller than **1**, suggesting even weaker SMM behaviour for **4**. To further estimate the magnetic exchange interaction (*J*) and the exchange spectrum, we have fitted the magnetic susceptibility and magnetization data using the Lines model implemented in the POLY_ANISO code. The POLY_ANISO code has been successfully used to simulate the magnetic properties of highly anisotropic polynuclear complexes.[53, 54] The magnetic exchange interactions (exchange + dipole) between Dy(III) centres were modelled by $\hat{H} = -(J_{exch} + J_{dip})S_{1z}S_{2z}$ where J_{exch} and J_{dip} are the exchange and dipolar coupling, respectively, while S_{1z} and S_{2z} are the projection of pseudo-spin S = ½ of the ground state KD of Dy1 and Dy2 centres. The best fit of the experimental magnetic susceptibility and magnetization data yields the $J_{tol} = -0.01$ cm^{-1} (J_{exch} = 0.009 cm^{-1} and J_{dip} = -0.019 cm^{-1}). The exchange and dipolar interactions are opposite in sign, with a significant contribution coming from dipolar interactions. The observed g_{zz} axes at Dy1 and Dy2 centers are arranged antiparallel, which is in line with the observed antiferromagnetic dipolar interaction. The computed exchange spectrum indicates suppression of QTM within the ground state, compared to the single-ion level; however, we do not see a substantial increase in the U_{cal} values (see Figure 15(c)).

DISCUSSION AND CONCLUSION

In summary, we have utilized a rigid pentadentate chelating ligand (H_2L) as the basis ligand to isolate a series of octacoordinate mononuclear Dy(III) complexes, [Dy(L)(Ph_3PO)(OOCR)] (where R = C_6H_5 (**1**), $C(CH_3)_3$ (**2**), CF_3 (**3**)) and a dinuclear complex, [$Dy_2(L)_2(Ph_3PO)_2\{(OOC)_2C_6H_4\}$] (**4**) employing TPPO and carboxylates as anciliiary ligands. Single-crystal X-ray diffraction studies confirmed the molecular structures of the complexes. The cumulative coordination action of the dianionic pentadentate ligand $[L]^{2-}$, TPPO and the carboxylate ligands generates the mononuclear and the dinuclear species. The $[L]^{2-}$ ligand coordinates to the Dy(III) center in a planar chelating coordination mode. The TPPO occupies one side of this planar geometry and the other side is occupied by the carboxylate ligands in a chelating coordination mode. Static and dynamic magnetic measurements were performed on the polycrystalline solid samples of **1**–**4**. Complex **1** shows SMM behavior at zero applied magnetic fields with a relaxation mechanism dominated by a thermally activated process, with Δ = 39 (2) K (τ_0 = 2.7(6) x 10^{-6} s). Complex **2** shows SMM behavior at a relatively small applied magnetic field with Δ = 15.8(2) K (τ_0 = 3.9(3) x 10^{-7} s (H_{DC} = 500 Oe). Complex **3** shows slow relaxation of magnetization at an applied magnetic field of 1000 Oe; the dynamics is dominated by the Raman relaxation process. Slow relaxation of magnetization is also observed in complex **4** under zero applied magnetic field, the magnetization relaxation dynamics being dominated by Raman and Quantum Tunneling relaxation processes. Detailed theoretical studies also corroborate the observed experimental behaviour.

EXPERIMENTAL SECTION

Materials and methods. The reagents and solvents were obtained from commercial sources and used as received. The ligand 2,6-diacetylpyridine *bis*-benzohydrazone (H_2L) was synthesized following a reported procedure.[55] FT-IR spectra were obtained using a Bruker

FT-IR spectrometer. Elemental analyses of the compounds were obtained using a Euro Vector EA instrument (CHNS-O, Model EuroEA3000). A powder X-ray diffraction study was performed on a finely ground polycrystalline material with RIGAKU Smartlab X-ray diffractometer at operational power of 9kW with Hypix-3000 detector.

Magnetic Measurements. Magnetic measurements were performed using a Quantum Design MPMS3 magnetometer. Magnetization measurements at different fields at a given temperature confirm the absence of ferromagnetic impurities. The sample was blocked in eicosane to avoid orientation under strong magnetic fields. Data were corrected for the sample holder and eicosane and diamagnetism was estimated from Pascal constants.

X-ray crystallographic studies. The single-crystal X-ray diffraction data of **1**–**4** were collected using a XtaLAB AFC12 (RINC) Kappa single diffractometer equipped with a fine-focus sealed X-ray tube to generate MoKα radiation (λ = 0.71073 Å). The crystals were kept at 120(10) K during data collection. Data were collected and integrated using the *CrysAlisPro* software.[56] Empirical absorption correction of the data was subsequently performed using spherical harmonics implemented in SCALE3 ABSPACK scaling algorithm in the *CrysAlisPro* software.[56] Using Olex2,[57] the structure was solved with the SHELXT[58] structure solution program using Intrinsic Phasing and refined with the SHELXL[59] refinement package using Least Squares minimization. All the non-hydrogen atoms were refined with anisotropic thermal parameters. All the hydrogen atoms were included in calculated positions and refined using a riding model. The "OLEX-2/MASK" command was used to get rid of the electron densities arising from heavily disordered solvents which could not be modelled satisfactorily.[60, 61] All the mean plane analyses and crystallographic figures have been generated using the DIAMOND software (version 3.2k).[62] The supramolecular interactions were calculated using the PLATON software and the respective graphical representations were generated in the DIAMOND softwere.[60, 62] The crystal data and

refinement parameters for **1**–**4** are summarized in Table 4. More details on the crystallographic data are given in the X-ray crystallographic files in the CIF format.

Synthesis

General procedure. The following general protocol was employed for the synthesis of complexes **1**–**4**.

The ligand H_2L (1 eq.) was suspended in 20 mL of EtOH and to it triphenyl phosphine oxide (TPPO) (1 eq.) and the respective carboxylic acid (1 eq.) were added. To this white suspension, solid $DyCl_3 \cdot 6H_2O$ (1 eq.) was added which resulted in a yellow solution. The reaction mixture was then heated under reflux for 2 h and allowed to cool to room temperature. To this solution NEt_3 (3 eq.) was added and the solution was further stirred at room temperature for 15 minutes. From this reaction mixture the solvent was stripped off in vacuo. The resulting yellow precipitate was washed with diethyl ether. The dried yellow precipitate was then dissolved in 15 mL of EtOH/$CHCl_3$ (1:2 v/v) and filtered. The filtrate was kept for slow evaporation to afford, after one week, yellow block-shaped crystals suitable for X-ray crystallography. The stoichiometry of the reactants involved in each reaction, yield of the products, and their characterization data are provided below:

*[(L)Dy(Ph_3PO)(OOCPh)] (**1**).* H_2L (0.060 g, 0.150 mmol), Ph_3PO (0.042 g, 0.150 mmol), PhCOOH (0.018 g, 0.150 mmol), $DyCl_3 \cdot 6H_2O$ (0.057 g, 0.150 mmol), and Et_3N (63 μL, 0.450 mmol) were used. Yield: 0.105 g, 68% (based on Dy). M.P.: >250 °C. IR (KBr ν/cm^{-1}): 3445(br), 3053(m), 2915(w), 1620(w), 1593(m), 1553(m), 1536(s), 1505(s), 1437(m), 1418(s), 1369(s), 1327(m), 1300(m), 1260(w), 1197(w), 1162(s), 1120(m), 1092(m), 1068(m), 1041(m), 998(w), 987(m), 942(w), 916(w), 898(w), 853(m), 809(m), 743(m), 720(s), 693(s) 680(m), 618(w), 541(s). Anal. Calcd for $C_{48}H_{39}Dy_1N_5O_5P_1$ (959.34): C, 60.10; H, 4.10; N, 7.30. Found: C, 59.88; H, 4.26; N, 7.14.

*[(L)Dy(Ph_3PO)($OOCC(CH_3)_3$)] (**2**).* H_2L (0.060 g, 0.150 mmol), Ph_3PO (0.042 g, 0.150 mmol), ^tBuCOOH (17 µL, 0.150 mmol), $DyCl_3 \cdot 6H_2O$ (0.057 g, 0.150 mmol), and Et_3N (63 μL, 0.450 mmol) were used. Yield: 0.099 g, 67% (based on Dy). M.P.: >250 °C. IR (KBr ν/cm-1): 3443(br), 3056(w), 2958(m), 2917(w), 2865(w), 1588(s), 1554(s), 1528(s), 1502(s), 1485(s), 1425(s), 1368(s), 1326(m), 1299(m), 1259(w), 1225(w), 1167(s), 1119(m), 1093(m), 1067(m), 896(m), 812(m), 750(m), 714(s), 694(s) 608(w), 538(s). Anal. Calcd for $C_{46}H_{43}Dy_1N_5O_5P_1$ (939.35): C, 58.82; H, 4.61; N, 7.46. Found: C, 58.67; H, 4.53; N, 7.28.

*[(L)Dy(Ph_3PO)($OOCCF_3$)] (**3**).* H_2L (0.060 g, 0.150 mmol), Ph_3PO (0.042 g, 0.150 mmol), CF_3COOH (12 μL, 0.150 mmol), $DyCl_3 \cdot 6H_2O$ (0.057 g, 0.150 mmol), and Et_3N (63 μL, 0.450 mmol) were used. Yield: 0.090 g, 63% (based on Dy). M.P.: >250 °C. IR (KBr ν/cm^{-1}): 3430(br), 3057(m), 2919(w), 1708(m), 1681(m), 1652(s), 1587(s), 1555(s), 1505(s), 1446(m), 1437(s), 1413(s), 1364(s), 1327(s), 1300(m), 1258(m), 1201(s), 1158(s), 1121(s), 1093(m), 1068(m), 1042(s), 990(m), 933(w), 916(w), 898(m), 853(m), 807(m), 750(m), 715(s), 694(s) 681(m), 652(w), 617(w), 539(s). Anal. Calcd for $C_{43}H_{34}Dy_1F_3N_5O_5P_1$ (951.24): C, 54.29; H, 3.60; N, 7.36. Found: C, 54.02; H, 3.39; N, 7.11.

*[Dy_2($L)_2$($Ph_3PO)_2${$(OOC)_2$}C_6H_4] (**4**).* H_2L (0.060 g, 0.150 mmol), Ph_3PO (0.042 g, 0.150 mmol), 1,4-$C_6H_4(COOH)_2$ (0.011 g, 0.075 mmol), $DyCl_3 \cdot 6H_2O$ (0.057 g, 0.150 mmol), and Et_3N (63 μL, 0.450 mmol) were used. Yield: 0.093 g, 67% (based on Dy). M.P.: >250 °C. IR (KBr ν/cm^{-1}): 3423(br), 3057(m), 2919(w), 1619(w), 1587(m), 1553(s), 1508(s), 1438(m), 1405(s), 1367(s), 1325(m), 1300(m), 1260(w), 1166(s), 1120(m), 1094(m), 1068(m), 1041(m), 988(w), 897(w), 840(m), 801(w), 751(m), 714(s), 693(s) 680(m), 650(w), 539(s). Anal. Calcd for $C_{90}H_{72}Dy_2N_{10}O_{10}P_2$ (1840.57): C, 58.73; H, 3.94; N, 7.61. Found C, 58.56; H, 3.76; N, 7.44.

Table 4. Crystallographic data and refinement parameters of **1**–**4**.

	1	**2**	**3**	**4**
Empirical formula	$C_{48}H_{39}Dy_1N_5O_5P_1.2CH_3OH$	$C_{46}H_{43}Dy_1N_5O_5P_1.CH_3OH$	$C_{43}H_{34}Dy_1F_3N_5O_5P_1$	$C_{90}H_{72}Dy_2N_{10}O_{10}P_2$
Formula weight	1023.42	971.39	951.22	1840.51

($gmol^{-1}$)				
Temperature (K)	120(10)	120.00(10)	120(10)	120.00(10)
Crystal system	Monoclinic	Monoclinic	Triclinic	Triclinic
Space group	*P*21/n	*C*c	*P*-1	*P*-1
Unit cell lengths (Å)	a = 13.1458(6) b = 22.4579(9) c = 15.9855(7)	a = 14.5520(7) b = 19.6201(9) c = 16.4532(8)	a = 11.1068(6) b = 11.8584(5) c = 16.9438(5)	a = 10.2273(3) b = 11.6932(3) c = 17.9065(5)
Unit cell angles (°)	α = 90 β = 105.613(4) γ = 90	α = 90 β = 108.729(5) γ = 90	α = 88.990(3) β = 83.329(3) γ = 62.514(5)	α = 90.766(2) β = 92.337(2) γ = 113.618(3)
Volume ($Å^3$)	4545.2(4)	4448.8(4)	1964.70(17)	1959.40(10)
Z	4	4	2	1
ρ_{calc} (g/cm^3)	1.402	1.402	1.608	1.560
Absorption coefficient	1.729	1.765	2.010	2.002
F(000)	1932.0	1900.0	950.0	924.0
Crystal size (mm^3)	0.3 × 0.15 × 0.08	0.39 × 0.17 × 0.16	0.24 × 0.13 × 0.10	0.15 × 0.12 × 0.1
Radiation	Mo Kα (λ = 0.71073)	Mo Kα (λ = 0.71073)	Mo Kα (λ = 0.71073)	Mo Kα (λ = 0.71073)
2θ range for data collection (°)	4.84 to 57.92	5.22 to 58.016	5 to 52.74	4.98 to 58.64
Reflections collected	49949	32964	31017	36772
Index ranges	-17 ≤ h ≤ 16, -30 ≤ k ≤ 24, -21 ≤ l ≤ 19	-19 ≤ h ≤ 18, -24 ≤ k ≤ 26, -21 ≤ l ≤ 22	-13 ≤ h ≤ 12, -14 ≤ k ≤ 14, -21 ≤ l ≤ 20	-14 ≤ h ≤ 12, -15 ≤ k ≤ 14, -24 ≤ l ≤ 24
Independent reflections	10709 [R_{int} = 0.0558]	9944 [R_{int} = 0.1009]	8005 [R_{int} = 0.0446]	9264 [R_{int} = 0.0545]
Data/Restrain/Parameter	10709/25/571	9944/27/544	8005/0/525	9264/0/516
Goodness-of-fit on F^2	1.091	1.017	1.041	1.096
Final R indices [I>2sigma(I)]	R_1 = 0.0323, wR_2 = 0.0670	R_1 = 0.0698, wR_2 = 0.1685	R_1 = 0.0302, wR_2 = 0.0654	R_1 = 0.0415, wR_2 = 0.0909
R indices (all data)	R_1 = 0.0437, wR_2 = 0.0697	R_1 = 0.0765, wR_2 = 0.1734	R_1 = 0.0353, wR_2 = 0.0678	R_1 = 0.0515, wR_2 = 0.0938
Largest diff. peak/hole / e $Å^{-3}$	0.72/-0.89	4.38/-2.49	1.00/-1.17	3.08/-1.14
Data completeness (2θ full)	99.8%	99.9%	99.8%	99.8%
CCDC Number	2313286	2313287	2313288	2313290

In order to check the phase purity of the complexes, powder X- ray diffraction measurement for complexes was done and found that the sequence and pattern of the peaks are in reasonable agreement with the simulated data obtained from single-crystal data (Figure S31).

Electronic Supplementary Information (ESI): Simulated single-crystal data and experimental XRD pattern for **1-4**, Molecular structures of **2-4**, Continuous Shape measurement calculations, coordination geometries, and Supramolecular interactions of **1-4**, Cole-Cole plot for **1-4**, In-phase (*left*) and out-of-phase (*right*) susceptibility curves for complex **2-4** under various applied DC fields, the Frequency dependence of χ''_M at different temperatures for **2** under an applied magnetic field, Cole-Cole plot for **3** under zero applied

magnetic field, LoProp charge around the Dy centers, Computed Loprop charge for the complex **1-4**, SINGLE_ANISO computed crystal field parameters for **1, 2, 3** and **4,** and POLY_ANISO Simulation Results for the complexes**.**

ACKNOWLEDGMENTS

V.C. is thankful to the Dept. of Science and Technology, New Delhi, India, for a National J. C. Bose Fellowship. P.K. is thankful to Tata Institute of Fundamental Research, Hyderabad for postdoctoral fellowship. S.K.S. acknowledges the Department of Science and Technology for the Start-up Research Grant CRG/2023/002936 and IIT Hyderabad for generous funding. K.K. thanks PMRF for the Ph.D. fellowship. The support and resources provided by the PARAM Seva Facility at the Indian Institute of Technology, Hyderabad, are gratefully acknowledged.

Notes

The authors declare no competing financial interest.

REFERENCES

1. L. Sorace, C. Benelli and D. Gatteschi, *Chem. Soc. Rev.*, 2011, **40**, 3092-3104.

2. J.-C. G. Bünzli, *J. Coord. Chem.*, 2014, **67**, 3706-3733.

3. C. Huang, *Rare earth coordination chemistry fundamentals and applications*, Wiley, Singapore, 2010.

4. A. d. Bettencourt-Dias, *Luminescence of lanthanide ions in coordination compounds and nanomaterials*, John Wiley & Sons Inc., United Kingdom, 2014.

5. N. Ishikawa, M. Sugita, T. Ishikawa, S.-y. Koshihara and Y. Kaizu, *J. Am. Chem. Soc.*, 2003, **125**, 8694-8695.

6. D. N. Woodruff, R. E. P. Winpenny and R. A. Layfield, *Chem. Rev.*, 2013, **113**, 5110-5148.

7. J. Tang and P. Zhang, *Lanthanide Single Molecule Magnets*, Springer-Verlag GmbH, Berlin 2016.

8. R. Layfield and M. Murugesu, *Lanthanides and Actinides in Molecular Magnetism*, Wiley-VCH, Germany, 2015.

9. K. Bernot, *Molecular magnetism of lanthanides complexes and networks*, MDPI, Switzerland, 2018.

10. R. A. Layfield, *Organometallics*, 2014, **33**, 1084-1099.

11. O. Kahn, *Molecular Magnetism*, Wiley-VCH, New York, 2001.

12. C. Benelli and D. Gatteschi, *Introduction to Molecular Magnetism From Transition Metals to Lanthanides*, Wiley-VCH, Germany 2015.

13. R. J. Blagg, L. Ungur, F. Tuna, J. Speak, P. Comar, D. Collison, W. Wernsdorfer, E. J. L. McInnes, L. F. Chibotaru and R. E. P. Winpenny, *Nat. Chem.*, 2013, **5**, 673.

14. J.-L. Liu, Y.-C. Chen and M.-L. Tong, *Chem. Soc. Rev.*, 2018, **47**, 2431-2453.

15. Z. Zhu, M. Guo, X.-L. Li and J. Tang, *Coord. Chem. Rev.*, 2019, **378**, 350-364.

16. J. Lu, M. Guo and J. Tang, *Chem. Asian J.*, 2017, **12**, 2772-2779.

17. P. Zhang, L. Zhang, C. Wang, S. Xue, S.-Y. Lin and J. Tang, *J. Am. Chem. Soc.*, 2014, **136**, 4484-4487.

18. P. Zhang, L. Zhang and J. Tang, *Dalton Trans.*, 2015, **44**, 3923-3929.

19. A. K. Bar, P. Kalita, M. K. Singh, G. Rajaraman and V. Chandrasekhar, *Coord. Chem. Rev.*, 2018, **367**, 163-216.

20. P. Zhang, Y.-N. Guo and J. Tang, *Coord. Chem. Rev.*, 2013, **257**, 1728-1763.

21. L. Spree and A. A. Popov, *Dalton Trans.*, 2019, **48**, 2861-2871.

22. V. S. Parmar, D. P. Mills and R. E. P. Winpenny, *Chem. Eur. J.*, 2021, **27**, 7625-7645.

23. L. Maxwell, M. Amoza and E. Ruiz, *Inorg. Chem.*, 2018, **57**, 13225-13234.

24. J. D. Rinehart and J. R. Long, *Chem. Sci.*, 2011, **2**, 2078-2085.

25. L. Ungur and L. F. Chibotaru, *Inorg. Chem.*, 2016, **55**, 10043-10056.

26. L. Ungur and L. F. Chibotaru, *PCCP*, 2011, **13**, 20086-20090.

27. N. F. Chilton, *Inorg. Chem.*, 2015, **54**, 2097-2099.

28. G. K. G. Jack Emerson-King, George F. S. Whitehead, Iñigo J. Vitorica-Yrezabal, Mathieu Rouzières, Rodolphe Clérac, Nicholas F. Chilton, David P. Mills, *ChemRxiv* 2023, DOI: 10.26434/chemrxiv-2023-xv0ht

29. Y.-C. Chen, J.-L. Liu, L. Ungur, J. Liu, Q.-W. Li, L.-F. Wang, Z.-P. Ni, L. F. Chibotaru, X.-M. Chen and M.-L. Tong, *J. Am. Chem. Soc.*, 2016, **138**, 2829-2837.

30. J. Liu, Y.-C. Chen, J.-L. Liu, V. Vieru, L. Ungur, J.-H. Jia, L. F. Chibotaru, Y. Lan, W. Wernsdorfer, S. Gao, X.-M. Chen and M.-L. Tong, *J. Am. Chem. Soc.*, 2016, **138**, 5441-5450.

31. Y.-S. Ding, N. F. Chilton, R. E. P. Winpenny and Y.-Z. Zheng, *Angew. Chem. Int. Ed.*, 2016, **55**, 16071-16074.

32. S. K. Gupta, T. Rajeshkumar, G. Rajaraman and R. Murugavel, *Chem. Sci.*, 2016, **7**, 5181-5191.

33. C. R. Ganivet, B. Ballesteros, G. de la Torre, J. M. Clemente-Juan, E. Coronado and T. Torres, *Chem. Eur. J.*, 2013, **19**, 1457-1465.

34. X.-L. Ding, Y.-Q. Zhai, T. Han, W.-P. Chen, Y.-S. Ding and Y.-Z. Zheng, *Chem. Eur. J.*, 2021, **27**, 2623-2627.

35. A. B. Canaj, S. Dey, E. R. Martí, C. Wilson, G. Rajaraman and M. Murrie, *Angew. Chem. Int. Ed.*, 2019, **58**, 14146-14151.

36. C. A. Gould, K. R. McClain, D. Reta, J. G. C. Kragskow, D. A. Marchiori, E. Lachman, E.-S. Choi, J. G. Analytis, R. D. Britt, N. F. Chilton, B. G. Harvey and J. R. Long, *Science*, 2022, **375**, 198-202.

37. P. Kalita, N. Ahmed, A. K. Bar, S. Dey, A. Jana, G. Rajaraman, J.-P. Sutter and V. Chandrasekhar, *Inorg. Chem.*, 2020, **59**, 6603-6612.

38. P. Kalita, N. Ahmed, S. Moorthy, V. Béreau, A. K. Bar, P. Kumar, P. Nayak, J.-P. Sutter, S. K. Singh and V. Chandrasekhar, *Dalton Trans.*, 2023, **52**, 2804-2815.

39. A. K. Bar, P. Kalita, J.-P. Sutter and V. Chandrasekhar, *Inorg. Chem.*, 2018, **57**, 2398-2401.

40. V. E. Campbell, H. Bolvin, E. Rivière, R. Guillot, W. Wernsdorfer and T. Mallah, *Inorg. Chem.*, 2014, **53**, 2598-2605.

41. Y.-N. Guo, L. Ungur, G. E. Granroth, A. K. Powell, C. Wu, S. E. Nagler, J. Tang, L. F. Chibotaru and D. Cui, *Sci. Rep.*, 2014, **4**, 5471.

42. Z.-H. Li, Y.-Q. Zhai, W.-P. Chen, Y.-S. Ding and Y.-Z. Zheng, *Chem. Eur. J.*, 2019, **25**, 16219-16224.

43. A. B. Canaj, S. Dey, C. Wilson, O. Céspedes, G. Rajaraman and M. Murrie, *Chem. Commun.*, 2020, **56**, 12037-12040.

44. V. Singh, D. Das, S. Anga, J.-P. Sutter, V. Chandrasekhar and A. K. Bar, *ACS Omega*, 2022, **7**, 25881-25890.

45. *SHAPE: Continuous Shape Measures calculation*, Electronic Structure Group, Universitat de Barcelona, Spain, version 2.1, 2013.

46. J. Cirera, E. Ruiz and S. Alvarez, *Organometallics*, 2005, **24**, 1556-1562.

47. C. R. Martinez and B. L. Iverson, *Chem. Sci.*, 2012, **3**, 2191-2201.

48. M. Nishio, *CrystEngComm*, 2004, **6**, 130-158.

49. L. Ungur and L. F. Chibotaru, *Chem. Eur. J.*, 2017, **23**, 3708-3718.

50. B. O. Roos, P. R. Taylor and P. E. M. Sigbahn, *Chem. Phys.*, 1980, **48**, 157-173.

51. S. K. Singh, C. J. Cramer and L. Gagliardi, *Inorg. Chem.*, 2020, **59**, 6815-6825.

52. I. Tarannum, S. Moorthy and S. K. Singh, *Dalton Trans.*, 2023, **52**, 15576-15589.

53. J. Acharya, N. Ahmed, J. Flores Gonzalez, P. Kumar, O. Cador, S. K. Singh, F. Pointillart and V. Chandrasekhar, *Dalton Trans.*, 2020, **49**, 13110-13122.

54. D. Shao, P. P. Sahu, W.-J. Tang, Y.-L. Zhang, Y. Zhou, F.-X. Xu, X.-Q. Wei, Z. Tian, S. K. Singh and X.-Y. Wang, *Dalton Trans.*, 2022, **51**, 18610-18621.

55. C. Pelizzi and G. Pelizzi, *J. Chem. Soc., Dalton Trans.*, 1980, DOI: 10.1039/DT9800001970, 1970-1973.

56. *CrysAlisPro* Rigaku Americas Coorporation, The Woodlands, Texas, USA, version 1.171.39.29d, 2017.

57. O. V. Dolomanov, L. J. Bourhis, R. J. Gildea, J. A. K. Howard and H. Puschmann, *J. Appl. Crystallogr.*, 2009, **42**, 339-341.

58. G. M. Sheldrick, *Acta Crystallogr. A*, 2015, **71**, 3-8.

59. G. M. Sheldrick, *Acta Crystallogr. C*, 2015, **71**, 3-8.

60. A. Spek, *J. Appl. Crystallogr.*, 2003, **36**, 7-13.

61. P. van der Sluis and A. L. Spek, *Acta Crystallogr. A*, 1990, **46**, 194-201.

62. H. Putz and K. Brandenburg, *DIAMOND*, Crystal Impact GbR, Bonn, Germany, version version 3.2, 1997−2014.

TOC Graphic:

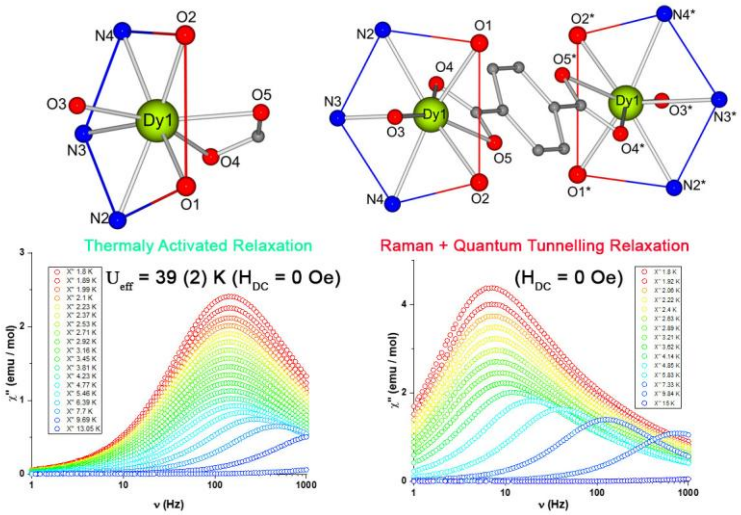

A series of octa-coordinate mononuclear Dy(III) complexes, [Dy(L)(Ph_3PO)(OOCR)] (where R = C_6H_5 (**1**), $C(CH_3)_3$ (**2**), CF_3 (**3**)) and a dinuclear complex, [$Dy_2(L)_2(Ph_3PO)_2${$(OOC)_2C_6H_4$}] (**4**) were synthesized using a rigid pentadentate chelating ligand (H_2L). Complexes **1** and **4** showed SMM behaviour under zero DC field.